Applied Physics Letters

Controlling the spatio-temporal dose distribution during STEM imaging by subsampled acquisition: *In-situ* observations of kinetic processes in liquids

Cite as: Appl. Phys. Lett. **115**, 063102 (2019); https://doi.org/10.1063/1.5096595
Submitted: 19 March 2019 . Accepted: 18 June 2019 . Published Online: 05 August 2019

B. L. Mehdi, A. Stevens, L. Kovarik, N. Jiang, H. Mehta, A. Liyu, S. Reehl, B. Stanfill, L. Luzi, W. Hao, L. Bramer, and N. D. Browning

AIP Publishing

Applied Physics Letters ARTICLE scitation.org/journal/apl

Controlling the spatio-temporal dose distribution during STEM imaging by subsampled acquisition: *In-situ* observations of kinetic processes in liquids

Cite as: Appl. Phys. Lett. **115**, 063102 (2019); doi: 10.1063/1.5096595
Submitted: 19 March 2019 · Accepted: 18 June 2019 ·
Published Online: 5 August 2019

B. L. Mehdi,[1,2,a)] A. Stevens,[3] L. Kovarik,[4] N. Jiang,[5] H. Mehta,[4] A. Liyu,[4] S. Reehl,[6] B. Stanfill,[6] L. Luzi,[6] W. Hao,[2] L. Bramer,[6] and N. D. Browning[1,2,3]

AFFILIATIONS

[1]Department of Mechanical, Materials and Aerospace Engineering and Department of Physics, University of Liverpool, Liverpool L69 3GH, United Kingdom
[2]Physical and Computational Science Directorate, PNNL, Richland, Washington 99352, USA
[3]Sivananthan Laboratories, Bolingbrook, Illinois 60440, USA
[4]Environmental Molecular Sciences Laboratory, PNNL, Richland, Washington 99352, USA
[5]Department of Physics, Arizona State University, Tempe, Arizona 85281, USA
[6]National Security Directorate, PNNL, Richland, Washington 99352, USA

[a)]**Author to whom the correspondence should be addressed:** b.l.mehdi@liverpool.ac.uk

ABSTRACT

Subsampled image acquisition followed by image inpainting in a scanning transmission electron microscope is a novel approach to control dose and increase the image frame rate during experiments, thereby allowing independent control of the spatial and temporal dose envelope during image acquisition. Here, subsampled imaging is shown to permit precise *in situ* observations of the fundamental kinetic processes behind nucleation and growth of silver (Ag) nanoparticles from an aqueous solution. At high sampling-levels, nanoparticles can be observed with morphologies that are consistent with strong interface interactions, i.e., rafts and pillars, whereas at low sampling-levels, the particles exhibit regular spherical morphologies. The relative numbers of rafts/pillars and regular nanoparticles, their sizes, and their incubation times can be attributed to local changes in the molar concentration of the Ag ions in the aqueous solution; higher sampling-levels significantly increase the reactants in the vicinity of the window, leading to rapid supersaturation and the precipitation on the window surface. These precisely controlled kinetics highlight subsampled imaging as a method by which the driving force for nucleation and growth (i.e., the electron beam) can be disentangled from the spatial/temporal resolution of the observation in all *in situ* experiments, providing a pathway to identify and quantify the importance of individual kinetic factors behind nucleation and growth in a wide variety of complex materials systems and architectures.

The nucleation and growth of nanostructures from solution have important consequences for materials synthesis,[1] mineralization,[2] atmospheric conditions and climate change,[3] interactions with biological interfaces,[4] and energy storage[5] to name but a few applications. Nucleation is in general described by classical nucleation theory,[6] where the rate of nucleation is determined by the overall energy cost of nucleating a new phase. Nucleation of a second phase, such as the formation of ice in water, can also be affected by the presence of a secondary interface; when there is no interface involved and a nanoparticle is precipitated from solution directly, it is termed homogeneous nucleation, while precipitation in the presence of an interface is termed heterogeneous nucleation. Heterogeneous nucleation generally can proceed more rapidly, as the presence of the interface lowers the energy barrier for precipitating the second phase. In addition to these classical nucleation modes, it is becoming increasingly clear that nonclassical pathways for nucleation also exist, such as the formation of intermediate amorphous phases.[7] Once a particle is nucleated, then the growth mechanism also becomes important, with a classical Ostwald ripening molecular attachment mechanism being modified by other effects such as particle agglomeration[8] and oriented attachment.[9] Hence, while nucleation and growth are fundamental to many scientific fields and models for the basics of the process have been developed over many years, there are clearly intricate details and nuances that can apply to understanding what happens in each materials system, which warrants a closer experimental study.

The recent development of *in situ* liquid stages for high-resolution (scanning) transmission electron microscopes (S/TEM) has provided a direct means to observe nucleation and growth phenomena in materials under various driving forces.[10–15] For example, in the studies of silver (Ag) metal nanoparticles nucleating in aqueous solution by Woehl *et al.*[8,15] it was found that individual nanoparticles follow an Ostwald ripening mechanism consistent with classical nucleation theory. However, as growth continues, the particle size distribution is dominated by a Smoluchowski agglomeration mechanism. Further work in this area by Welch *et al.*[16] identified that particles going beyond agglomeration to coalesce are dominated by an oriented attachment effect where the effect of the solvent shield around the nanoparticles promotes tip-to-tip attachment. In these studies (and all observations using *in situ* liquid cells generated by the TEM community so far), the resolution of the images that have been obtained has been limited by the effect of the electron beam changing the local chemistry of the solution. While nucleation and growth are typically triggered by the electron beam, if the electron dose is too high, then the liquid breaks down forming radicals and eventually extensive gas bubbles.[17] To increase the spatial and temporal resolution of these *in situ* observations in the liquid stage, it is therefore imperative to use imaging methodologies that extract the most information from the least amount of electron dose put into the cell.

The recent application of subsampling and inpainting to STEM imaging offers one potential way of extracting quantitative information from images acquired with fewer pixels.[18–22] Notably, acquiring fewer pixels can both decrease dose and increase frame rates depending on the beam conditions. In subsampled imaging, the image is formed by only acquiring a small random fraction of the pixels in the image and then using inpainting (related to compressive sensing recovery methods[23,24]) to fill in the missing information. While there are limitations in how quickly the scan can currently be performed, the practical application of subsampled acquisitions can clearly lead to improved dose/resolution relationships for STEM images.[18] In this paper, we use these subsampling methods to demonstrate that subsampled microscopy can lead to high quality fast imaging during an *in situ* experiment. In addition, the use of subsampling allows the fundamental kinetics of the nucleation and growth process to be identified directly by separating the intrinsic image resolution from the electron dose conditions that typically swamp standard microscopy observations.

A 0.1 mM $AgNO_3$ solution was prepared and illuminated with a wide range of electron doses and subsampling rates to induce nucleation and growth (a full description of the chemical preparation and the subsampling and inpainting procedures are given in the supplementary material).

Figure 1 shows frames from the reconstructed videos (videos are included in the supplementary material as is a full description of the subsampling and inpainting process) at 100%, 25%, 12%, and 3% of the pixels acquired. The electron beam current remains constant across each sampling-level, meaning that the electron dose in each acquisition is scaled down by the degree of subsampling from the full sampled image dose. As can be seen from the raw acquisitions, the reduction in dose significantly changes the rate of growth (see supplementary material videos, SM1–4). Moreover, there are 3 distinct structural forms of the precipitates that exist in these experiments—each of which is clearly visible in the video frames (Fig. 2).

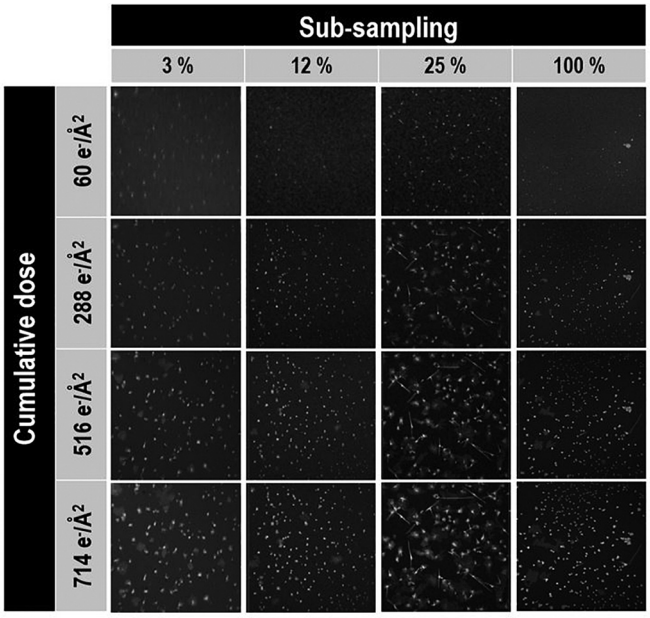

FIG. 1. A set of subsampled images taken from different cumulative doses (i.e., time stamps) in the *in situ* nucleation and growth of Ag nanoparticles. For each of the images, the cumulative dose is controlled by the magnification, scan speed, and subsampling of the images. The videos from which these images were taken are shown in the supplementary material (SM1).

The first type of shape visible in the images is a uniform almost spherical or facetted square structure, which has uniform contrast across the majority of the nanoparticle—which we term as a "regular" particle here. We use Z-contrast imaging to form the image, as this type of nanoparticle has uniform thickness, and it is likely that these nanoparticles are as thick as they are wide. The second type of nanoparticle observed is one that is larger than the first in terms of area but has much less contrast in the image, indicating that it is a flat structure or "raft." The third and final type of particle is a thin needle looking structure that has a very high intensity compared to the others, which we term as a "pillar." The pillars and rafts both appear to be 2-D in nature but grow at 90° to each other.

From the segmentation of the images shown in Fig. 2, we can track the nucleation and growth of the 3 types of particles as a function of the sampling rate (a description of the image analytics used for this measurement is given in the supplementary material). To fit to the experimental observations, we will use the Finke-Watzky (F-W) model[25] shown in the following equation:

$$A(t) = w\left(1 - \frac{1 + \frac{k_1}{k_2 w}}{1 + \frac{k_1}{k_2 w}\exp[(k_1 + k_2 w)t]}\right). \quad (1)$$

This model has been shown to be equivalent to or better than the more widely used Avrami approach,[25] and the parameters have a more intuitive interpretation: $A(t)$ is the converted volume at time t, w is the final volume, k_1 is a "nucleation" rate, and k_2 is a "growth" rate (the fitting parameters and the normalized error for the plots

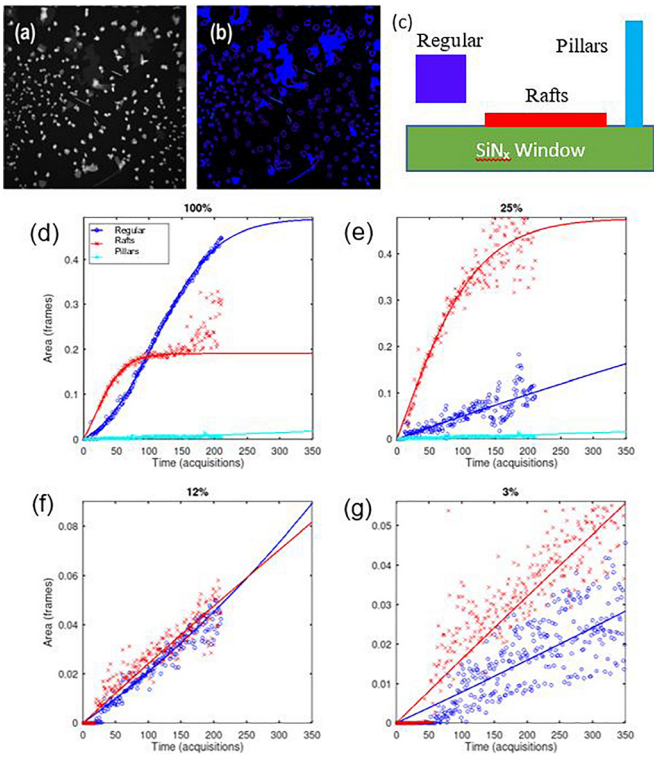

FIG. 2. (a) The reconstructed image can be segmented (b) to track the development of the 3 types of nanoparticles unambiguously identified from the mass-thickness contrast in the Z-contrast image as regular, raft, and pillar (c). Analysis of the nucleation and growth rate for the 3 nanoparticle types using the F-W model in Eq. (1) (A full description of the segmentation and tracking process is given in the supplementary material.) for (d) 100% sampling, (e) 25% sampling, (f) 12% sampling, and (g) 100% sampling. For the lower doses, the particles are still growing at the end of the experiment, whereas for the higher sampling, the particles are constant by the end of the experiment. There is a clear separation between the modes for higher sampling rates which reduces significantly for the lower sampling rates.

shown in Fig. 2 are given in supplementary material Tables ST1–4). We note that there are some limitations in this approach since the nucleation and growth parameters of each particle type are modeled separately, rather than treating them as competitive processes, and we do not have an accurate measure of the thickness (volume) of each particle. The F-W interpolations of the experimental data in Fig. 2 allow the differences in parameters between the different types of particles to be identified (Fig. 3). Importantly, these experimental results fall into two clear groups, with the dividing line being above 12% sampling.

To assess these differences in growth kinetics, we compare the fitting results for each type of structure across each sampling-level (Fig. 3). The regular particles appear to show similar nucleation and growth rates for each sampling-level, indicating that the conditions for the formation of these particles (i.e., both the nucleation energy-barrier and the Ag-ion flux) are relatively constant across each experiment. The results in Fig. 3 also clearly demonstrate that while there is no difference in the incubation time of the raft structures (which nucleate almost immediately), the growth rate for raft structures is faster at higher sampling-levels. This suggests that the nucleation barrier is similar for each experiment but that there is a larger flux of Ag

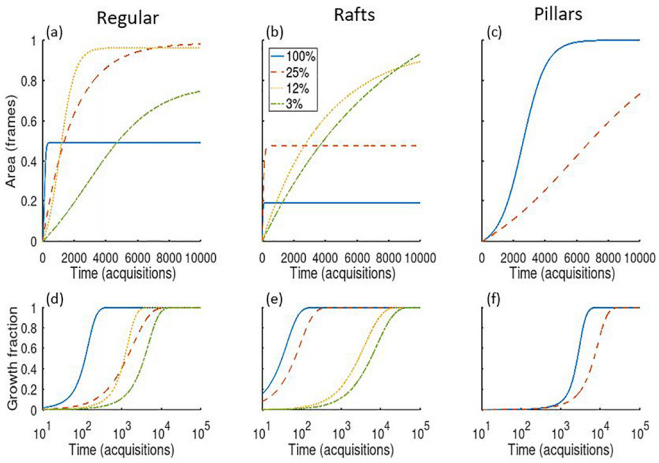

FIG. 3. Comparison of the growth rate as a function of sampling for (a) the regular particles, (b) the rafts and (c) the pillars as a function of the total number of frames, and (d), (e), and (f) as a function of the total experimental time. There are clearly 3 different modes of nucleation and growth in each experiment, and the differences depend on the sampling rate.

ions for the growth of these raft structures in the highly sampled experiments. The dendrites also have an incubation time that scales with the sampling rate, but in this case, they are only seen to occur for the highest levels of sampling (both 100% and 25%) and appear to grow after and between the rafts.

Given that we have unambiguously identified 3 different nanoparticle structures that are nucleated during the experiment and that the fit to the F-W model shows that each one has different nucleation/growth constants depending on the sampling rate, we can now ask the question as to what is it about the *in situ* experiment that could be causing this. In this regard, a recent paper by Jiang[26] showed that when the high energy electron beam passes through an insulator such as the SiN_x window, it can create secondary electrons, which in turn creates an electric field at the surface of that insulator. For the *in situ* cell, of course, one of the surfaces of the insulating window is the interface between the window and the nominally conducting aqueous solution and the presence of a field at this interface should change the distribution of the charged ions in solution.

An example of the type of field created in the region of the STEM probe is shown in Fig. 4, where an increase in the gradient of the electric field is observed at both the upper and lower SiN_x windows of the *in situ* liquid STEM cell (in any real microscopy experiment, the upper window would experience more primary electrons, making the field higher than at the bottom window). We can estimate what effect this has on the ions that are created in the reaction solution using the Nernst-Planck equation,

$$\frac{\partial c}{\partial t} = -D\nabla \cdot [\nabla c + mzF\, c(\nabla \phi)]. \tag{2}$$

Figure 4 shows a COMSOL finite element simulation of the distribution of ions in solution under different illumination conditions. While it is very difficult to calculate exactly how many secondary electrons are produced in each experiment and the cross section for radiolysis is not known, we can model the effects of a high beam dose concentration vs

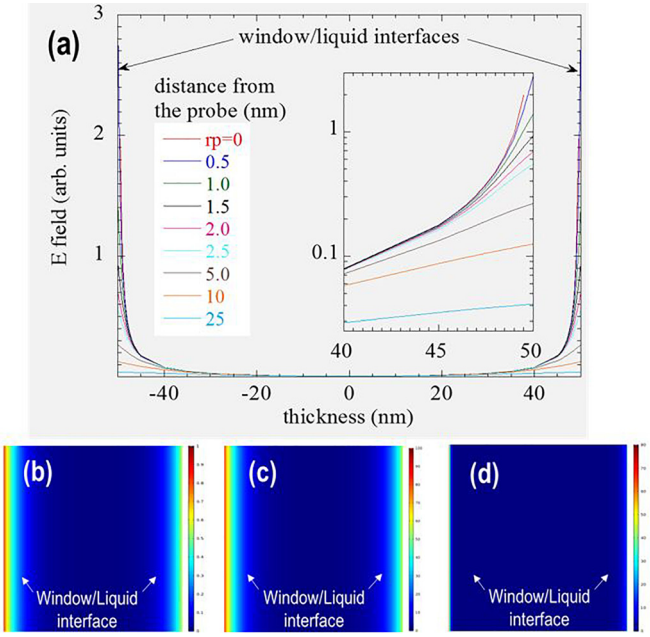

FIG. 4. (a) Simulations of the electric field increase at the windows caused by illumination by the electron beam. The amount of increase is directly related to dose (dose rate)—the higher the electron dose (dose rate), the larger the build-up of secondary electrons and the larger the field. COMSOL finite element simulation for the increase in concentration at the interface for (b) a low field (0.2 V) and low starting concentration (0.1 M), (c) a low field (0.2 V) and high starting concentration (10 M), and (d) a high field (2 V) and higher starting concentration (1 M). In all cases, the role of the field is to increase the concentration of reactants at the windows.

low beam dose concentration and high initial solution concentration vs low initial solution concentration to understand the differences in these *in situ* experiments. The results show that at a given concentration of the $AgNO_3$ solution, the effect of the electron beam always causes an increase in the concentration of the reactants directly in the window area. As the field depends on the integrated dose, the only way to reduce this effect is to minimize the spatiotemporal distribution of the dose. This has an additional effect on the reaction process by reducing the number of Ag ions that are released from solution—the creation of Ag ions is also a function of the beam dose concentration. For controlled formation of nanoparticles, we can see that the low dose concentration regime of the subsampling has multiple benefits. It has been noted previously that reactions in *in situ* cells proceed faster than expected[27] from the initial solution concentration, and this is clearly a result of the concentrating effect at the windows. This effect is also why reactions are seen in liquid cells even when the dose is high enough to cause a bubble.[28] The bubble will form in the middle of the solution, leading to the decrease in the liquid thickness with all the reactants being further pushed toward the window surface. Even liquid thicknesses of a few nanometers should still show nucleation and growth behavior in the cell (also shown in supplementary material Fig. S1 is a Z-contrast image showing the nanoparticles from other experiments all either being on the top window or bottom window of the cell).

Having established that the liquid-window interface is important during these *in situ* experiments, we can now interpret our observations of the formation of regular, raft, and pillar structures in terms of the presence of this interface. For the regular particles, the fact that they have an incubation time longer than the rafts and are essentially unchanged in growth rate with sampling strongly suggests that these are particles nucleated outside of the increased concentration zone around the window shown in Fig. 4 and are homogeneously nucleated. Since the raft structures nucleate first, appear to be 2-D in nature, and have a growth rate that is proportional to the sampling, it can be concluded that these particles arise from heterogeneous nucleation on the windows. It is known from the preparation of supported gold catalysts that when the oxide support is doped with electrons, then the gold islands form as rafts rather than as spherical particles.[29] The explanation for this is that the Au atoms have a stronger electron affinity than they do to form bonds with other Au atoms, causing them to form islands a single atom thick on the surface of the support. Although the electron affinity of Ag is not as high as Au, a similar mechanism may be taking place here. When the subsampling reaches a high enough level, the doping of the interface is such that it is energetically more favorable for the Ag atoms to form a raft than it is for them to form homogeneous particles. Such an effect would be consistent with classical nucleation theory where the interaction with the support decreases the surface energy and promotes more rapid growth of 2-D structures rather than 3-D structures. In the case of the pillars, they only form toward the end of the most highly sampled experiments. Obviously, in the case of the fully sampled acquisition, there is a high supersaturation of reactants in the vicinity of a very high electric field at the liquid-window interface. Under these circumstances, the precipitation and a "dendritic growth" mechanism[30] are not surprising and are completely consistent with the pillar growth that is observed here.

In summary, these results show that both subsampling and inpainting can provide an advantageous means to obtain high resolution images of the kinetics behind nucleation and growth during dynamic *in situ* liquid experiments. While the focus of this work was originally to highlight the increase in speed obtained by this approach, it has also demonstrated that control of the sampling can allow the kinetic parameters at interfaces to be isolated and controlled. This has far reaching implications for the study of interface reactions in a wide variety of complex heterostructured systems where the material can be patterned on the window and the concentration of reactants locally controlled by the sampling of the image. These *in situ* STEM methods combined with subsampled acquisition can therefore be a powerful tool in unlocking interface interactions and dynamic ion exchange processes.

See the supplementary material for the experimental movies, the subsampling/inpainting procedure, and the fitting parameters for the F-W model.

The development of Compressive sensing for EM applications was supported by the Chemical Imaging Initiative, a Laboratory Directed Research and Development Program at Pacific Northwest National Laboratory (PNNL). PNNL is a multiprogram national laboratory operated by Battelle for the U. S. Department of Energy (DOE) under Contract No. DE-AC05-76RL01830. A portion of the research was performed using the Environmental Molecular Sciences Laboratory (EMSL), a national scientific user facility sponsored by the Department of Energy's Office of Biological and Environmental Research and located at PNNL.

REFERENCES

[1]A. R. Tao, S. Habas, and P. Yang, Small **4**, 310–325 (2008).
[2]C. M. Hansel, S. G. Benner, and S. Fendoirf, Environ. Sci. Technol. **39**, 7147–7153 (2005).
[3]M. Kulmala, H. Vehkamuki, T. Petaja, M. Del Maso, A. Lauri, V. M. Kerminen, W. Birmili, and P. H. McMurry, J. Aerosol Sci. **35**, 143–176 (2004).
[4]J. L. Gardea-Torresdey, J. G. Parsons, E. Gomez, J. Videa-Peralta, H. E. Troiani, P. Santiago, and M. J. Yacaman, Nano Lett. **2**, 397–401 (2002).
[5]R. Bhattacharyya, B. Key, H. L. Chen, A. S. Best, A. F. Hollenkamp, and C. P. Grey, Nat. Mater. **9**, 504–510 (2010).
[6]I. M. Lifshitz and V. V. Sloyozov, Chem. Solids **19**, 35–50 (1961).
[7]J. J. De Yoreo, P. Gilbert, N. A. J. M. Sommerdijk, R. L. Penn, S. Whitelam, D. Joester, H. Z. Zhang, J. D. Rimer, A. Navrotsky, J. F. Banfield, A. F. Wallace, F. M. Michel, F. C. Meldrum, H. Colfen, and P. M. Dove, Science **349**, aaa6760 (2015).
[8]T. J. Woehl, C. Park, J. E. Evans, I. Arslan, W. D. Ristenpart, and N. D. Browning, Nano Lett. **14**(1), 373–378 (2014).
[9]D. S. Li, M. H. Nielsen, J. R. I. Lee, C. Frandsen, J. F. Banfield, and J. J. De Yoreo, Science **336**, 1014–1018 (2012).
[10]M. J. Williamson, R. M. Tromp, P. M. Vereecken, R. Hull, and F. M. Ross, Nat. Mater. **2**(8), 532–536 (2003).
[11]H. M. Zheng, R. K. Smith, Y. W. Jun, C. Kisielowski, U. Dahmen, and A. P. Alivisatos, Science **324**(5932), 1309–1312 (2009).
[12]Y. Liu, K. P. Tai, and S. Dillon, Chem. Mater. **25**(15), 2927–2933 (2013).
[13]A. V. Levlev, S. Jesse, T. J. Cochell, R. R. Unocic, V. A. Protopopescu, and S. V. Kalinin, ACS Nano **9**, 11784–11791 (2015).
[14]B. L. Mehdi, J. Qian, E. Nasybulin, C. Park, D. A. Welch, R. Faller, H. Mehta, W. A. Henderson, W. Xu, C. M. Wang, J. E. Evans, J. Liu, J. G. Zhang, K. T. Mueller, and N. D. Browning, Nano Lett. **15**(3), 2168–2173 (2015).
[15]T. J. Woehl, J. E. Evans, I. Arslan, W. D. Ristenpart, and N. D. Browning, ACS Nano **6**(10), 8599–8610 (2012).
[16]D. A. Welch, T. J. Woehl, C. Park, R. Faller, J. E. Evans, and N. D. Browning, ACS Nano **10**, 181–187 (2016).
[17]F. M. Ross, Science **350**(6267), aaa9886 (2015).
[18]A. Stevens, H. Yang, L. Carin, L. I. Arslan, and N. D. Browning, Microscopy **63**(1), 41–51 (2014).
[19]L. Kovarik, A. Stevens, A. Liyu, and N. D. Browning, Appl. Phys. Lett. **109**, 164102 (2016).
[20]A. Béché, B. Goris, B. Freitag, and J. Verbeeck, Appl. Phys. Lett. **108**, 093103 (2016).
[21]R. Leary, Z. Saghi, P. A. Midgley, and D. J. Holland, Ultramicroscopy **131**, 70–81 (2013).
[22]M. Ferroni, A. Signoroni, A. Sanzogni, L. Masini, A. Migliori, L. Ortalani, A. Pezza, and V. Morandi, Sci. Rep. **6**, 33354 (2016).
[23]E. J. Candes, J. Romberg, and T. Tao, IEEE Trans. Inf. Theory **52**(2), 489–509 (2006).
[24]D. L. Donoho, IEEE Trans. Inf. Theory **52**(4), 1289–1306 (2006).
[25]E. E. Finney and R. G. Finke, Chem. Mater. **21**, 4692–4705 (2009).
[26]N. Jiang, Ultramicroscopy **179**, 81–83 (2017).
[27]T. J. Woehl, K. L. Jungjohann, J. E. Evans, I. Arslan, W. D. Ristenpart, and N. D. Browning, Ultramicroscopy **127**, 53–63 (2013).
[28]J. P. Patterson, P. Abellan-Baeza, M. S. Denny, Jr., C. Park, N. D. Browning, S. M. Cohen, J. E. Evans, and N. C. Gianneschi, JACS **137**, 7322–7328 (2015).
[29]X. Shao, S. Prada, L. Giordano, G. Pacchioni, N. Nilius, and H. J. Freund, Angew. Chem. **50**, 11525–11527 (2011).
[30]J. S. Langer and H. Muller-Krumbhaar, Acta Metall. **26**, 1681–1687 (1978).